Neutral Vortex Necklace in a Trapped Planar Superfluid

M. M. Cawte[1] · M. T. Reeves[2] · A. S. Bradley[1]

Abstract

We study quantum vortex states consisting of a ring of vortices with alternating sign, in a homogeneous superfluid confined to a circular domain. We find an exact stationary solution of the point vortex model for the neutral vortex necklace. We investigate the stability of the necklace state within both the point-vortex model and the Gross–Pitaevskii equation describing a trapped atomic Bose–Einstein condensate at low temperature. The point-vortex stationary states are found to also be stationary states of the Gross–Pitaevskii equation provided the finite thickness of the outer fluid boundary is accounted for. Under significant perturbation, the Gross–Pitaevskii evolution and point-vortex model exhibit instability as expected for metastable states. The perturbed vortex necklace exhibits sensitivity to the perturbation, suggesting a route to seeding vortex chaos or quantum turbulence.

Keywords Vortex · Bose–Einstein condensate · Superfluid

1 Introduction

The point-vortex model (PVM) of planar fluid motion [1, 2] provides a fascinating window into fluid dynamics; it offers an approximate model of normal fluid turbulence [3], and finds a rigorous manifestation in planar superfluids [4–6] where vorticity is quantized to integer multiples of h/m, where h is Planck's constant and m is the atomic mass. Dilute gas Bose–Einstein condensate (BEC) provide a favorable system in which to realize PVM physics. Precision confinement, forcing, and imaging of vortices in BECs have enabled experimental studies of vortex dipoles [7], the von Karman vortex street [8], and observations of Onsager's negative-temperature vortex cluster states [5, 6]. The PVM regime can be approximately realized

✉ A. S. Bradley
  ashton.bradley@otago.ac.nz

1   Dodd-Walls Centre for Photonic and Quantum Technologies, Department of Physics, University of Otago, Dunedin 9016, New Zealand

2   ARC Centre of Excellence in Future Low-Energy Electronics Technologies (FLEET), School of Mathematics and Physics, University of Queensland, St. Lucia, QLD 4072, Australia

in an atomic BEC, despite the compressible nature of the BEC superfluid [9, 10]. Advances in spatiotemporal control [11, 12] allow disc-shaped hard-wall traps to be created with dynamic laser manipulation [13]. Such advances offer exquisite control of the creation and placement of quantum vortices, and may soon enable systematic experimental study of dynamics and statistical mechanics in quasi-homogeneous systems [14–20], or forcing tailored to drive an inverse-energy cascade [10, 21].

A number of interesting links between stationary point-vortex systems in the infinite plane and the roots of special orthogonal polynomials [22] have been identified, including to Hermite [23], Laguerre [24], and Adler–Moser [25] polynomials. Yet the stationary and periodic solutions in the disc have received less attention. In this work, we find an exact analytical solution of the PVM describing a class of neutral vortex necklace states in a disc-confined atomic BEC. The neutral vortex necklace is determined by the roots of a quadratic polynomial related to the *metallic means*, a generalization of the golden ratio. We compare the exact PVM solutions with dynamical simulations of the Gross–Pitaevskii equation (GPE), finding that the stationary states in the PVM are also stationary GPE solutions, provided a small correction is applied to allow for the finite thickness of the fluid boundary. We also carry our further simulations of the GPE for weakly and highly deformed vortex necklace states and compare with simulations in the PVM.

The structure of the paper is as follows. We first review the PVM in Sect. 2. In Sect. 3, we derive the stationary solution for the neutral vortex necklace. In Sect. 4, we present our simulations of the vortex necklace and its perturbations, comparing the PVM and GPE results. In Sect. 5, we conclude.

2 Point Vortices

2.1 Background

Chiral Systems Systems of vortices with only one sign of circulation have been the subject of intense study due to their importance in superconductors and superfluid ground states. The most well-known stationary configuration of same-sign vortices is the Abrikosov lattice, a rigidly rotating periodic array with six-fold rotational symmetry that forms the energetic ground state in a rotating frame. Excited states in the rotating frame are chiral N-gon states [26], shown in a bounded domain in Fig. 1. While the $N + 1$-gon for $N = 6$ has the same symmetry as the Abrikosov lattice, it is only a particular case of a general class of stationary solutions that are not energetic ground states, but rather form metastable equilibrium solutions. General existence proofs for periodic equilibria in bounded domains have been challenging, emerging only recently [27–30].

Neutral Systems Systems with an equal number of positive and negative circulating vortices are much less studied, and play a central role in two-dimensional quantum turbulence where stirring a superfluid naturally injects vortex dipoles. Kuhl provides a general method for constructing vortex equilibria in any bounded, multiply connected domain with n-fold rotational symmetry [31]. However, while quite general, the construction is rather opaque. Confining our attention
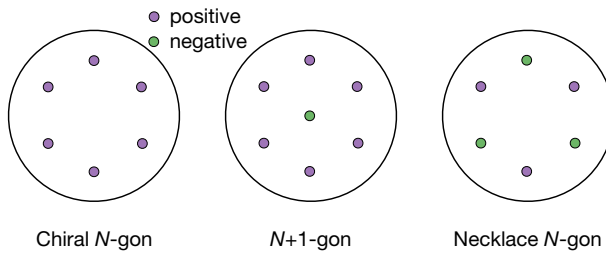
Fig. 1 Schematic of vortex N-gon, $N + 1$-gon, and Necklace N-gon states confined to a disc, for $N = 6$. The chiral state rotates rigidly without a change in shape, and the $N + 1$-gon and necklace are stationary non-rotating configurations in the laboratory frame. In each case, in the appropriate rotating frame the net force on each vortex due to the system boundary and the other vortices vanishes (Color figure online)

to a disc-shaped domain, we examine neutral systems with even vortex number N. For a neutral $N = 2$ system confined to a disc of radius R, the maximum energy state is also the stationary state, with the vortices lying along a common axis, at $x_{\pm} = \pm R/(2 + \sqrt{5})^{1/2} \approx 0.486R$; this case has been studied theoretically [19, 32–34], and experimentally [7, 35]. For $N \geq 4$, the stationary state is no longer the maximum energy vortex configuration. A particular stationary state may be constructed by placing each vortex symmetrically in a ring around the center of the trap with alternating circulations, creating a neutral vortex necklace. For $N \geq 4$, vortex necklaces have been studied theoretically in parabolic traps [33, 34, 36–38], and a constructive method of solution for arbitrary N in this common BEC confinement is provided by Barry et al. [39]. In the present work, we take an alternate approach to finding exact stationary solutions to the PVM for necklace N-gon states in a disc geometry with a hard wall boundary.

2.2 Point-Vortex Model

The equations of motion for N point vortices in the plane are given by [1]

$$\begin{pmatrix} \dot{x}_i \\ \dot{y}_i \end{pmatrix} = \frac{1}{2\pi} \sum_{j=1}^{N} {}' \frac{\Gamma_j}{r_{ij}^2} \begin{pmatrix} -y_{ij} \\ x_{ij} \end{pmatrix}, \tag{1}$$

where the prime on the summation denotes $j \neq i$, $\Gamma_j = \kappa_j h/m$ is the circulation, $\kappa_j \in \{-1, 1\}$ provides the sign of circulation, $x_{ij} = x_i - x_j$, and $r_{ij}^2 = (x_i - x_j)^2 + (y_i - y_j)^2$. As shown by Kirchhoff [2], these equations of motion can be restated in Hamiltonian form

$$\Gamma_i \dot{x}_i = \frac{\partial H}{\partial y}, \quad \Gamma_i \dot{y}_i = -\frac{\partial H}{\partial x}, \tag{2}$$

where x_i are the generalized coordinates and $p_i = \Gamma_i y_i$ are the generalized momenta conjugate to x_i. Converting to complex coordinates with $z_j = x_j + iy_j$ and subtracting off the infinite self-energy term gives the interaction Hamiltonian

$$H(z_1, \ldots, z_N) = -\frac{1}{2\pi} \sum_{i=1}^{N-1} \sum_{j=i+1}^{N} \Gamma_i \Gamma_j \log |z_i - z_j|. \tag{3}$$

In addition to the energy, in the disc domain the point-vortex angular momentum

$$I = \sum_i \Gamma_i r_i^2, \tag{4}$$

is also conserved.

Lin [40, 41] extended the dynamical equations to include bounded, simply-connected domains. For a disc of radius R, the method of images may be applied where each vortex has a corresponding image vortex with opposite circulation outside the disc at position $z_i^{im} = R/z_i^*$, where $z_j^* = x_j - iy_j$. The Hamiltonian becomes

$$H(z_1, \ldots, z_N) = -\frac{1}{4\pi} \left[\sum_{i=1, j\neq i}^{N} \Gamma_i \Gamma_j \log \frac{|z_i - z_j|}{|R^2 - z_i z_j^*|} - \sum_j^N \Gamma_j^2 \log\left(R^2 - |z_j|^2\right) \right], \tag{5}$$

and the equation of motion for vortex i is

$$\dot{z}_i^* = \frac{1}{2\pi i} \left[\sum_{j=1, i\neq j}^{N} \frac{\Gamma_j}{z_i - z_j} - \sum_{j=1}^{N} \frac{\Gamma_j z_j^*}{R^2 - z_j^* z_i} \right]. \tag{6}$$

The boundary terms allow for interesting stationary configurations involving a balance of intervortex forces and boundary forces.

3 Necklace N-gon: Exact Solution

We seek the N-fold rotationally symmetric stationary solution for N point-vortex dipoles in the disc. We denote the position of each vortex in the disc as

$$z_n = d_N e^{i2\pi(n-1)/N} \tag{7}$$

where $n = 1, 2, 3 \ldots$ is the vortex label, the signs $\kappa_n = (-1)^n$ arrange vortices in alternating circulation, d_N is the radial distance from the origin, and N is the total number of vortices which is always an even integer; the precise dependence of d_N on N will be found. Substituting the vortex locations and the alternating circulation into the equation of motion (6) for the first vortex gives

$$\dot{z}_1^* = -i\frac{\Gamma}{2\pi} \left[\sum_{n=2}^{N} \frac{\kappa_n}{z_1 - z_n} - \sum_{n=1}^{N} \frac{\kappa_n z_n^*}{R^2 - z_n^* z_1} \right], \tag{8}$$

The stationary states have $\dot{z}_n^* = 0$ for all vortices, giving the equation

$$0 = \sum_{n=2}^{N} \frac{\kappa_n}{z_1 - z_n} - \sum_{n=1}^{N} \frac{\kappa_n z_n^*}{R^2 - z_n^* z_1}, \tag{9}$$

Due to the symmetry of the necklace and the disc geometry, we only require the stationary solution for one vortex. Since the first vortex sits on the positive x-axis, $z_1 = d_N$, the steady state equation can be written as

$$S_1 + S_2 = 0, \tag{10}$$

where the two sums

$$S_1 \equiv \sum_{n=2}^{N} \frac{\kappa_n}{1 - e^{i2\pi(n-1)/N}} = \frac{1}{2}, \tag{11}$$

$$S_2 \equiv -\left(\frac{d_N}{R}\right)^2 \sum_{n=1}^{N} \frac{\kappa_n e^{-i2\pi(n-1)/N}}{1 - (d_N/R)^2 e^{-i2\pi(n-1)/N}} = \frac{N(R/d_N)^N}{1 - (R/d_N)^{2N}}, \tag{12}$$

are due to intervortex and image vortices, respectively. Both sums are non-trivial to perform; the proofs are given in "Appendix A". Using (11), (12), Eq. (10) becomes

$$x^2 - 2Nx - 1 = 0, \tag{13}$$

where $x = (R/d_N)^N$. The positive root yields $x = N + \sqrt{N^2 + 1}$, and the solution

$$d_N = \frac{R}{\left[N + \sqrt{N^2 + 1}\right]^{1/N}}, \tag{14}$$

for the radial distance from the origin of the vortex necklace (the negative root locates the ring of image vortices.[1] The solution uniquely determines a class of N-fold rotationally symmetric vortex necklace states as stationary solutions of the point vortex equations of motion in a disc domain. We note that it is also possible two write this exact solution in terms of a generalization of the golden ratio φ, given by the positive root of the quadratic equation $\varphi^2 - \varphi - 1 = 0$, namely $\varphi \equiv (1 + \sqrt{5})/2$. The quadratic equation can be used to develop a continued fraction for φ:

$$\varphi = 1 + \cfrac{1}{1 + \cfrac{1}{1 + \cfrac{1}{1 + \dots}}}. \tag{15}$$

A generalization of the golden ratio known as the metallic mean was introduced by de Spinadel [42]

---

[1] In preparing this manuscript we discovered that this analytical result was found using a different approach in the doctoral thesis of Q. Dai [30].

Fig. 2 Vortex necklace radius for increasing N. Also shown (red line) is the solution for large N given by $R/(2N)^{1/N}$, which is already a very good approximation for $N = 4$ (Color figure online)
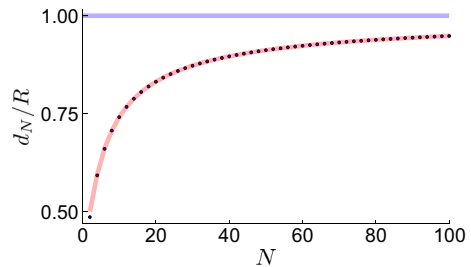
$$\Phi_n = n + \cfrac{1}{n + \cfrac{1}{n + \cfrac{1}{n + \ldots}}} = \frac{n + \sqrt{n^2 + 4}}{2}, \tag{16}$$

where $n \in \mathbb{N}$ and the n-th metallic mean, Φ_n, is the positive root of $\Phi_n^2 - n\Phi_n - 1 = 0$. The first few metallic means are referred to as the identity (0-th), the golden (first), silver (second), and bronze (third) ratio.

We note a useful approximation to the exact solution that will almost always be applicable. For a single dipole, $N = 2$, and $d_2 = R/(2 + \sqrt{5})^{1/2} \approx 0.4859R$. However, for large $N \gg 1$,

$$d_N \simeq \frac{R}{(2N)^{1/N}} \left[1 + \mathcal{O}\left(\frac{1}{N}\right) \right], \tag{17}$$

moving ever closer to the domain boundary at R as N increases. This behavior is shown in Fig. 2, where it may also be seen that the approach to $d_N \to R/(2N)^{1/N}$ is very fast, with an error of only 0.5% for $N = 4$. From Eq. (13), we see that in terms of the metallic means the necklace states can be written as $d_N = R/\sqrt[N]{\Phi_{2N}}$; for large $N \gg 1$ (16) shows that $\Phi_{2N} \to 2N$, consistent with (17). Already for $N = 4$, $\Phi_{2N} \simeq 8.123 \approx 2N$, with an error of only $\sim 1.5\%$. Geometrically, the position of each vortex is determined by $2N - 1$ distances between the vortex, the $N - 1$ other vortices, and the N images imposed by the boundary. For $N \gg 1$ and $2N - 1 \approx 2N$, and the self-interaction is unimportant relative to all of the mutual interactions between vortices and images.

4 Simulations

The predictions of the PVM provide an approximation to the motion of vortices in a planar BEC confined by a hard-wall potential to a disc domain [5, 6]. In this section, we compare the exact PVM solutions with vortex dynamics governed by the Gross–Pitaevskii equation. We model a system of atoms held in a hard-wall trap that is otherwise homogeneous. The atomic density is thus homogeneous away from a sharp boundary, and the primary physics beyond the PVM stems from the compressibility of the quantum fluid; there is a small but non-negligible vortex core size set by the healing length. Closely related is the finite thickness of the boundary layer

of the fluid. In general, vortices can also couple to the phonon field supported by the BEC. Provided the healing length is small, as is the case in 2DQT systems, we may expect PVM and GPE to be in fairly close agreement [5]. However, it is not a priori clear how close the agreement will be, nor the nature of the departure. We examine the dynamics of the vortex necklace N-gon, both for initial conditions very near the point vortex stationary solution and for larger deformations of the vortex configuration.

4.1 Gross–Pitaevskii Equation

For the superfluid simulations we consider a BEC state described by wavefunction $\Psi(\mathbf{r}, t)$, and containing N atoms

$$\int d^3\mathbf{r} \ |\Psi(\mathbf{r}, t)|^2 = N. \tag{18}$$

Numerically, we solve the GPE [43]

$$i\hbar \frac{\partial \Psi(\mathbf{r}, t)}{\partial t} = \left(-\frac{\hbar^2}{2m} \nabla^2 + V_{\text{ext}}(\mathbf{r}, t) + g|\Psi(\mathbf{r}, t)|^2 \right) \Psi(\mathbf{r}, t), \tag{19}$$

where V_{ext} is the external potential, $g = 4\pi\hbar^2 a_s/m$ is the two-body interaction parameter, and a_s is the s-wave scattering length. We assume the system is tightly confined in the z direction so that the wavefunction is separable $\Psi(\mathbf{r}, t) \equiv \psi(x, y, t)\psi_0(z)$. Integrating over the z direction, the GPE for ψ assumes a 2D form, but with interaction parameter $g_{2D} = g \int |\psi_0|^4 dz$; here the ground state z wavefunction is a Gaussian normalized as $\int d^2\mathbf{r} \ |\psi_0|^2 = 1$. Defining the healing length

$$\xi \equiv \frac{\hbar}{\sqrt{m\mu}}, \tag{20}$$

where the chemical potential $\mu = g_{2D}n_0$ is determined by n_0, the homogeneous 2D atomic number density away from the steep $x - y$ confining potential. For the homogeneous system, it is convenient to work in units of length, time, and energy of ξ, ξ/c, and $\mu = \hbar^2/m\xi^2$ respectively, where $c \equiv \sqrt{g_{2D}n_0/m}$ is the speed of sound.

4.2 Initial Conditions

The disc-shaped hard-wall potential was constructed as

$$V_{\text{ext}}(x, y) = \begin{cases} 0, & \text{for } \sqrt{x^2 + y^2} < R, \\ 5\mu, & \text{for } \sqrt{x^2 + y^2} \geq R, \end{cases} \tag{21}$$

where R is the radius of the trap. The total dimensions of the system were $128\xi \times 128\xi$ with 512 grid points in each direction chosen to give high resolution inside the vortex cores. Each simulation was started with a fixed number of particles

in the external potential V_{ext} and evolved with imaginary time in order to find the ground state of the system without vortices, $\phi_0(\mathbf{r})$. It is not desirable to introduce any further imaginary time evolution of vortex configurations, as damping significantly alters the vortex positions for metastable states such as the vortex necklace.[2] Instead, we achieve an excellent approximation to any given vortex configuration by using a numerically exact single vortex solution together with linearity of the phase, to construct an accurate wavefunction ansatz. We construct a vortex state by applying density and phase imprinting to the ground state to create a wavefunction ansatz for the system, given by

$$\psi(\mathbf{r}) = \prod_{n=1}^{N} f(\mathbf{r} - \mathbf{r}_n) e^{i\varphi(\mathbf{r})} \phi_0(\mathbf{r}), \tag{22}$$

where $f(\mathbf{r})$ is the profile of a single vortex in a homogeneous background condensate computed numerically to high accuracy using a Chebyshev basis [44], $\mathbf{r}_n$ is the location of each vortex, and $\varphi(\mathbf{r})$ is the phase. For a necklace state with well-separated vortices, the solutions for the density profile of a single vortex may be multiplied together to create the density profile of the necklace state that gives a good approximation to the true solution. The location of each vortex in the necklace is given by

$$\mathbf{r}_n = (x_n, y_n) \equiv d_N[\cos(2\pi(n-1)/N), \sin(2\pi(n-1)/N)], \tag{23}$$

and the phase of the necklace state is given by

$$\varphi(x, y) = \sum_{n=1}^{N} e^{i\pi(n-1)} \left[\arctan\left(\frac{y - y_n}{x - x_n}\right) - \arctan\left(\frac{y - y_n^i}{x - x_n^i}\right) \right], \tag{24}$$

where $y_n^i \equiv y_n R^2/|d_N|^2$ and $x_n^i \equiv x_n R^2/|d_N|^2$ are the positions of the image vortices which enforce the condition that fluid cannot flow across the boundary. These functions are used to imprint phase profile and the vortex density onto the ground state condensate at each vortex location. The use of the exact density profile of the single vortex core means that there is almost no additional acoustic energy introduced during the vortex creation process.

4.3 Corresponding Units of Length, Time, and Energy Between PVM and GPE Simulations

Units of length, time, and energy may be chosen for the PVM simulations such that the vortex dynamics are comparable to the GPE simulations. This can be done by choosing the unit of length to be ξ, the unit of time to be $2\pi\xi^2/\Gamma$, and the unit of energy to be $\rho\Gamma^2/2\pi$ where the homogeneous condensate density and healing length are related by $\rho = m/2\pi\xi^2$.

---

[2] For similar reasons, it is not desirable to work in a rotating frame, as the neutral necklace is non-rotating.
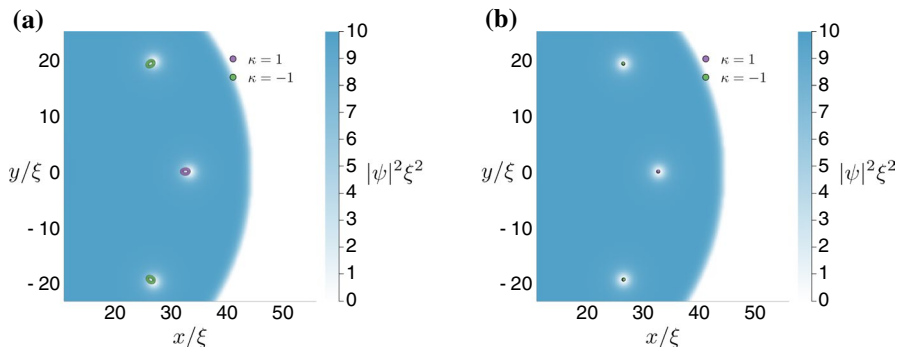
Fig. 3 GPE simulations of the $N = 10$ necklace state in a disc of radius $R = 45\xi$. The vortex trajectories are presented by a scatter plot superimposed on a heatmap of the initial particle density. **a** GPE simulation of the $N = 10$ necklace state after simulation duration $t = 2000\xi/c$. Each vortex in the necklace state orbits about a point on a length scale of about a healing length. **b** GPE simulation of the $N = 10$ necklace state radially perturbed inward by 0.6ξ after duration $t = 2000\xi/c$ (Color figure online)

Although this choice of units for the PVM gives vortex dynamics comparable to the GPE system with identical initial vortex positions, the fluid that the GPE describes is compressible and includes finite vortex core size and boundary effects. Hence, the dynamics in each model for simulations with the same duration of time should not be expected to be identical.

4.4 Computational Algorithms

The GPE and PVM were numerically integrated in the Julia programming language [45] with the `Tsit5` [46] algorithm from the `DifferentialEquations.jl` package [47]. The GPE was integrated using a pseudo-spectral Fourier method and vortices were created and detected using the `VortexDistributions.jl` package [48]. The vortex detection algorithm operates on a Cartesian grid with point spacing Δx, and uses an optimized version of plaquette detection (performing a phase loop integral around each grid plaquette of area $(\Delta x)^2$ to locate the vortex to a single plaquette, followed by local interpolation, to locate any vortex to better than $0.1\Delta x$ resolution.

4.5 Stationary and Quasi-Stationary States

The analytic solution to the necklace state was confirmed to be stationary in numerical PVM simulations. However, using the initial necklace state positions from the PVM in the GPE results in vortices with small periodic trajectories. As an example, we use the $N = 10$ necklace state whose initial vortex positions in the PVM are given by d_{10} (Eq. 14). A GPE simulation of this state is shown in Fig. 3a, in which the vortex trajectories process inward by 1.4ξ for many orbits. A correction to the PVM prediction for the necklace state is required as the condensate density must
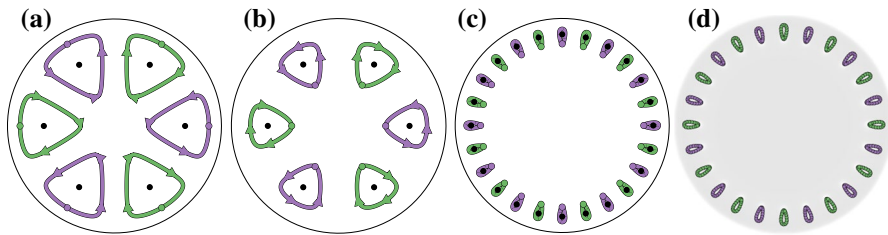
Fig. 4 Large deformations to the vortex necklace that conserve angular momentum. The stationary positions are marked in black, the deformed position is marked with a colored circle, and the arrows indicate the direction of motion. Each system is in a disc of radius $R = 45\xi$. **a** PVM simulation for 1 period of oscillation ($t \approx 1200\xi/c$) for the $N = 6$ necklace radially deformed outward by 10ξ. **b** PVM simulation for 1 period of oscillation ($t \approx 1519\xi/c$) for the $N = 6$ necklace state deformed radially inward by 10ξ. **c** PVM simulation for 1 period of oscillation ($t = 360\xi/c$) for the $N = 24$ necklace state deformed inward by 4ξ. **d** GPE simulation for 2.8 periods of oscillation for the $N = 24$ necklace state deformed inward by 4ξ. The simulation had a duration of $t = 1000\xi/c$. Here, the stationary positions marked in black are omitted for visual clarity and the lines are replaced by scattered points representing the location of the vortices through time (Color figure online)

smoothly transition from the homogeneous interior solution to zero outside the hard-wall potential, inducing a shift in the velocity field due to displaced image charges. The need for a boundary correction to improve the agreement between point-vortex and GPE simulations has also been reported in a study of binary BEC, involving a nonzero vortex core mass [49].

To numerically identify the boundary adjustment to the PVM solution, we performed GPE simulations for $N = [4, 6, 8, 10]$ necklace states in the $R = 45\xi$ trap, with radially symmetric perturbations to the initial positions in increments 0.1ξ over the interval -1ξ to 1ξ. As shown in "Appendix B", a small adjustment to the PVM solution (14) of less than ξ is sufficient to locate the GPE stationary solutions. We refer to this small perturbation as the boundary correction, and in the case of the $N = 10$ necklace state in Fig. 3b, we apply the boundary correction by radially perturbing the initial vortex positions inward by 0.6ξ. After a simulation of duration equal to that in Fig. 3a, the well-chosen boundary correction is seen to reduce the precession to be much less than ξ, imperceptible in the figure.

4.6 Angular Momentum Conserving Deformations

Non-perturbative, large-amplitude deformations of the vortex necklace states induce interesting quasi-periodic vortex dynamics. In the remainder of this work, we study two classes of deformations, comparing PVM and GPE simulations. In Fig. 4a, b, we show some simple deformations to the necklace state in the point-vortex model that preserve the angular momentum I, Eq. (4). The point-vortex angular momentum does not change because half of the Γ_i are positive and half are negative; hence, if the coordinate displacement is the same for all vortices, I is preserved. Angular momentum can be introduced only by breaking the cylindrical symmetry of the configuration. The vortex trajectories resulting from these two deformations trace out similar triangular orbits, with the outward deformation creating larger orbits.

We next construct the same kind of angular momentum conserving deformation to the $N = 24$ necklace state by radially perturbing the necklace state inward by 4ξ, but this time compare the dynamics between PVM and GPE evolution. The PVM dynamics are presented in Fig. 4c and the GPE dynamics in Fig. 4d. The vortex trajectories in both systems now trace out somewhat elliptical orbits, with a faster period of oscillation than the previous deformations. An outward deformation of the $N = 24$ necklace of magnitude 10ξ is unfeasible as the initial vortex positions would exit the system. An inward deformation of the same magnitude is unstable in GPE simulations; however, in PVM simulations it results in vortex trajectories tracing out large semi-triangular orbits.

4.7 Non-conserving Deformations: Bow-Star Perturbation

For vortices confined to a disk domain the only integrals of motion are H and I, and hence $N = 1, 2$ are the only integrable cases.[3] For any $N > 2$, the system can exhibit chaotic dynamics in the disk domain. Indeed, the vast majority of perturbations to the necklace state that do not conserve angular momentum produce chaotic trajectories. In this section, we present a particular perturbation to the necklace state that produces periodic trajectories that are qualitatively distinct from the previous orbits. This new perturbation turns out to be more sensitive to differences between the PVM and GPE theories of vortex dynamics in the disc domain. We find that correcting for the exterior boundary thickness again gives better agreement between PVM and GPE.

The perturbation of a necklace state of N vortices is produced by moving all vortices of one circulation radially inward by the constant $p_N e^{\pi/N}$, and all vortices of the opposite circulation radially outward by the constant $p_N e^{-\pi/N}$. With this choice of perturbation, the radially inward perturbed vortices trace out a periodic star-shaped trajectory with the number of vertices equal to N, and the radially outward perturbed vortices trace out a trajectory that loops around each vertex of the star in turn. We refer to the perturbation, discovered numerically, as the *bow-star perturbation*:

$$z_n = \sum_{n=1}^{N} \left[d_N + p_N e^{(-1)^{(n-1)}\pi/N} \right] e^{2\pi i(n-1)/N}. \tag{25}$$

Vortex trajectories resulting from the bow-star perturbation deviate from periodic behavior into chaos with small changes to initial conditions. Empirical approximations to p_N require many significant digits to produce the periodic bow-star trajectory. This bow-star perturbation may provide an interesting starting point for seeding vortex chaos.

An example of the bow-star perturbation in Eq. 25 with $N = 6$ is shown in Fig. 5, where the value of $p_6 = 4.003038160663878\ldots$ was found empirically. The PVM simulation in Fig. 5a resulting from this perturbation produces a regular motion in

---

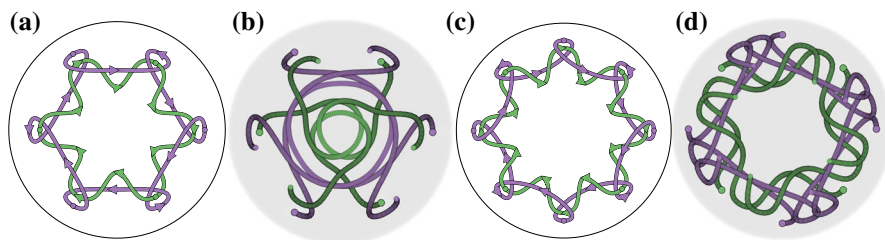[3] A detailed treatment of integrability is given by Newton [50].

Fig. 5 PVM and GPE simulations of $N = 6$ and $N = 8$ bow-star trajectories perturbed from the necklace state by Eq. 25. The lines in the PVM figures trace out the trajectories of the vortices through time with the arrows point in their direction of motion. The vortex trajectories in the GPE simulations are presented with scatter plots. The systems all have a disc of radius $R = 45\xi$. **a** PVM simulation of the $N = 6$ bow-star state for 3 periods of oscillation in which each vortex returns to its own initial position. The simulation had a duration of $t = 34,740\xi/c$. **b** GPE simulation of duration $t = 3260\xi/c$ for the $N = 6$ bow-star state. **c** PVM simulation of the $N = 8$ bow-star state for 2 periods of oscillation in which each vortex returns to its own initial position. The simulation had a duration of $t = 21,650\xi/c$. **d** GPE simulation of duration $t = 3240\xi/c$ for the $N = 8$ bow-star state (Color figure online)

which each vortex returns to its own initial position of period $t \approx 11,580\xi/c$. The negatively charged vortices trace out a six-pointed star and the positively charged vortices create a bow around the vertices of the star. The GPE simulation in Fig. 5b traces out a shape with the same "star" points and "bows", but each vortex rotates around the origin before tracing out the next star point or bow. Here, we only evolve the GPE simulation long enough to see the trajectories diverging from the PVM.

By creating the $N = 8$ necklace state with same perturbation from Eq. 25 but with $p_8 = 4.022725 \ldots$. The PVM simulation of the $N = 8$ bow-star in Fig. 5c has a period of $t \approx 10,825\xi/c$, whereby each vortex returns to its own initial position. In these dynamics, negatively charged vortices trace out an eight-pointed star, and the positively charged vortices create a bow around each star point. In the GPE simulation of the $N = 8$ bow-star in Fig. 5d, the negatively charged vortices trace out a shape close to a four-pointed star, with the bows from the positively charged vortices now in-between the stars. The shape becomes rotationally shifted before the first period.

As demonstrated in Fig. 3b, the necklace state in the GPE does not agree with the predictions of the necklace state from the PVM. By scanning over the parameter space a suitable correction to the necklace state in the GPE was found in "Appendix A". Although the bow-star trajectories are different between the PVM and GPE simulations, we may adjust the initial bow-star positions in the GPE by including the boundary correction

$$z_n = \sum_{n=1}^{N} \left[d_N - 0.6 + p_N e^{(-1)^{(n-1)}\pi/N} \right] e^{2\pi i(n-1)/N}. \tag{26}$$

The results of this adjustment to the initial positions of the bow-star state are shown in Fig. 6. The $N = 6$ bow-star with the boundary correction is shown in Fig. 6a after GPE evolution of duration $t = 4280\xi/c$. The trajectory is now much closer to that of the point-vortex trajectory in Fig. 5a, with the vortices tracing out an off-resonance
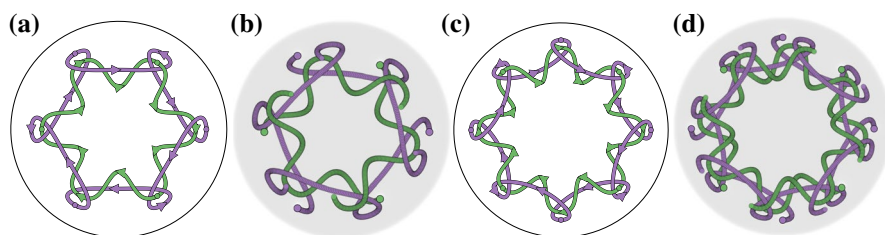
Fig. 6 $N = 6$ and $N = 8$ necklace states with the bow-star perturbation given in Eq. 25 and an inward radial perturbation of 0.6ξ applied. The lines in the PVM figures trace out the trajectories with arrows indicating direction. The vortex trajectories in the GPE simulations are presented with scatter plots (gray background). The systems all have a disc of radius $R = 45\xi$. **a** PVM simulation of the $N = 6$ bow-star state for 3 periods of oscillation in which each vortex returns to its own initial position. The simulation had a duration of $t = 34,743\xi/c$. **b** GPE simulation of the boundary corrected $N = 6$ bow-star state of duration $t = 4280\xi/c$. **c** PVM simulation of the $N = 8$ bow-star state for 3=2 periods of oscillation in which each vortex returns to its own initial position. The simulation had a duration of $t = 21,650\xi/c$. **d** GPE simulation of the boundary corrected $N = 8$ bow-star state of duration $t = 4045\xi/c$ (Color figure online)

six-pointed bow-star shape. In Fig. 5d, we see the $N = 8$ bow-star with corrected initial positions after GPE simulation of duration $t = 4045\xi/c$. The trajectory is now closer to that of the point-vortex trajectory in Fig. 5c, with the vortices tracing out an 8 pointed bow-star shape.

4.8 Non-neutral System

We have focused on the neutral system, but we note that our approach may also be used to find the stationary $N + 1$ vortex polygon, in which N vortices of the same circulation are placed in the disc radially symmetrically around a central vortex of oppositely signed circulation and varying strength.

The circulation of the ring vortices is given by $\Gamma_r = \kappa_r h/m$ where $\kappa_r \in \mathbb{R}$ is the strength and sign of circulation, and similarly $\Gamma_c = \kappa_c h/m$ for the central vortex which must have opposite sign compared to the radial vortices. The radial distance for the N vortices in the $N + 1$ vortex polygon is given by

$$d = R\left(\frac{2\kappa_c + \kappa_r N - \kappa_r}{2\kappa_c - \kappa_r N - \kappa_r}\right)^{\frac{1}{2N}}, \qquad (27)$$

provided $N \geq 2$ and the relation

$$\frac{\kappa_c}{\kappa_r} < \frac{(1 - N)}{2} \qquad (28)$$

is satisfied. In the PVM, vortex strengths of any real number are permitted provided Eq. 28 is satisfied. However, in a BEC vortices must have integer circulations and vortices with charge ≥ 2 are unstable. For example, by selecting $N = 2$, $\Gamma_r = -h/m$ for the radial circulations, and $\Gamma_c = h/m$ for the central vortex circulation, the

conditions required for a BEC system are satisfied with the distance of the radial vortices being $d = \sqrt[5]{4}$ plus a boundary correction.

5 Discussion and Conclusions

We have found an exact solution for the neutral vortex necklace in a planar super-fluid confined to a disc shaped domain. The radial locations of each vortex, due to a balance of forces from other vortices and the outer fluid boundary, can be written in terms of the *metallic mean*, a generalized golden ratio. We have tested the station-ary point-vortex solutions in simulations of the Gross–Pitaevskii equation, finding that a small radial adjustment, of order a healing length, yields a good approxima-tion to the metastable state for a dilute gas Bose–Einstein condensate. Comparing the dynamics of point vortex model and Gross–Pitaevskii equation, we find that large-scale deformations generate interesting symmetric and quasi-periodic vortex trajectories. The link between the form of perturbations and the transition between ordered periodic trajectories and chaos remains an interesting open question. Our results indicate that neutral vortex necklace may be an accessible metastable non-rotating state in atomic Bose–Einstein condensates, given sufficient vortex control, and may offer an interesting route to seed chaotic and turbulent vortex dynamics.

A Vortex Sums

Inter-Vortex Terms

The sum S_1 gives the contributions to the motion of z_1 from each of $N - 1$ vortices

$$S_1 = \sum_{n=2}^{N} \frac{e^{i\pi n}}{1 - e^{i2\pi(n-1)/N}}. \tag{29}$$

If the system being solved consists of a single dipole, then the total number of vorti-ces is $N = 2$ and the summation S_1 is reduced to the single term

$$S_1 = \left(\frac{e^{i\pi 2}}{1 - e^{i2\pi(2-1)/N}} \right) = \frac{1}{2}. \tag{30}$$

As we now show, this result holds for any even number of vortices. If the number of dipoles is greater than one, then we can shift the index of the summation and use the fact that the sum is always over an odd number of terms to find

$$S_1 = -\sum_{k=1}^{N-1} \frac{e^{i\pi k}}{1 - e^{i2\pi k/N}}$$

$$= -\left[\sum_{k=1}^{N/2-1} \frac{e^{i\pi k}}{1 - e^{i2\pi k/N}} + \frac{e^{i\pi N/2}}{1 - e^{i2\pi(N/2)/N}} + \sum_{k=N/2+1}^{N-1} \frac{e^{i\pi k}}{1 - e^{i2\pi k/N}} \right], \tag{31}$$

or

$$S_1 = -\frac{e^{i\pi N/2}}{2} - \left[\sum_{k=1}^{N/2-1} \frac{e^{i\pi k}}{1 - e^{i2\pi k/N}} + \sum_{k=N/2+1}^{N-1} \frac{e^{i\pi k}}{1 - e^{i2\pi k/N}} \right]. \tag{32}$$

The second sum can be cast in terms of the same index as the first. We first shift the index on the second sum

$$S_1 = -\frac{e^{i\pi N/2}}{2} - \left[\sum_{k=1}^{N/2-1} \frac{e^{i\pi k}}{1 - e^{i2\pi k/N}} + \sum_{k=1}^{N/2-1} \frac{e^{i\pi(k+N/2)}}{1 - e^{i2\pi(k+N/2)/N}} \right], \tag{33}$$

and then invert the order of summation by letting $l = N/2 - k$ and substituting it into the second sum, and finally relabel $l \rightarrow k$ to give

$$S_1 = -\frac{e^{i\pi N/2}}{2} - \sum_{k=1}^{N/2-1} \left[\frac{e^{i\pi k}}{1 - e^{i2\pi k/N}} + \frac{e^{i\pi(N-k)}}{1 - e^{i2\pi(N-k)/N}} \right]. \tag{34}$$

Using the fact that $e^{i\pi k} = e^{i\pi(N-k)}$ since N is even, we have

$$S_1 = -\frac{e^{i\pi N/2}}{2} - \sum_{k=1}^{N/2-1} e^{i\pi k} \left[\frac{1}{1 - e^{i2\pi k/N}} + \frac{1}{1 - e^{-i2\pi k/N}} \right]$$

$$= -\frac{e^{i\pi N/2}}{2} - \sum_{k=1}^{N/2-1} e^{i\pi k}$$

$$= \frac{(-1)^{N/2-1}}{2} - \sum_{k=1}^{N/2-1} e^{i\pi k}.$$

If $N/2 - 1$ is even, the first term is $1/2$ and the second is 0; if $N/2 - 1$ is odd the first term is $-1/2$ and the second is 1. Hence, $S_1 = 1/2$.

Vortex Image Terms

The second summation is the contribution from all of the vortex-images to the motion of the vortex z_1. It is given by

$$S_2 = -\left(\frac{d_N}{R} \right)^2 \sum_{n=1}^{N} \frac{\kappa_n e^{-i2\pi(n-1)/N}}{1 - (d_N/R)^2 e^{-i2\pi(n-1)/N}}. \tag{35}$$

To simplify, we let $a = (d_N/R)^2$

$$S_2 = -a \sum_{n=1}^{N} \frac{e^{i\pi n} e^{-i(n-1)2\pi/N}}{1 - ae^{-i(n-1)2\pi/N}} = a \sum_{k=0}^{N-1} \frac{e^{ik(N/2-1)2\pi/N}}{1 - ae^{-ik2\pi/N}}. \tag{36}$$

The geometric series Fourier transform pairs, valid for $a \neq 1$ are

$$\sum_{j=0}^{N-1} e^{-ijk2\pi/N} a^j = \frac{1 - a^N}{1 - ae^{-ik2\pi/N}}, \tag{37}$$

$$\frac{1}{N} \sum_{k=0}^{N-1} e^{ijk2\pi/N} \frac{1 - a^N}{1 - ae^{-ik2\pi/N}} = a^j, \tag{38}$$

where j can be chosen either positive or negative (the latter requiring $a \rightarrow a^{-1}$). Since we have initially made the choice $(-1)^k = e^{ik\pi}$, the transform (38) with positive choice $j \equiv N/2 - 1$ gives

$$a \sum_{k=0}^{N-1} \frac{e^{ik(N/2-1)2\pi/N}}{1 - ae^{-ik2\pi/N}} = aN \frac{a^{(N/2-1)}}{1 - a^N}, \tag{39}$$

with the result

$$S_2 = \frac{N(d_N/R)^N}{1 - (d_N/R)^{2N}}. \tag{40}$$

If we combine (11) and (40), Eq. (10) becomes

$$\frac{1}{2} + \frac{N(d_N/R)^N}{1 - (d_N/R)^{2N}} = 0, \tag{41}$$

or, in terms of $x = (d_N/R)^N$, the equation $x^2 - 2Nx - 1 = 0$, with positive root $x = N + \sqrt{N^2 + 1}$ giving

$$d_N/R = (N + \sqrt{N^2 + 1})^{1/N} > 1, \tag{42}$$

that describes the location of the images. The vortex locations are given by the second allowed choice for the phases: $(-1)^k = e^{ik\pi}$, and $j = -N/2 - 1$, instead giving the sum (12) and the location of the vortices (14).

B GPE Stationary States from Point-Vortex

In Fig. 7 the $N = 4, 6, 8, 10$ stationary PVM necklace state positions of the first vortex in each necklace are marked in yellow. To the left of each PVM stationary position marked in yellow, are the perturbed GPE trajectories of the first vortex in each necklace simulated over duration $t = 2000\xi/c$. To the left of the $N = 4$, PVM
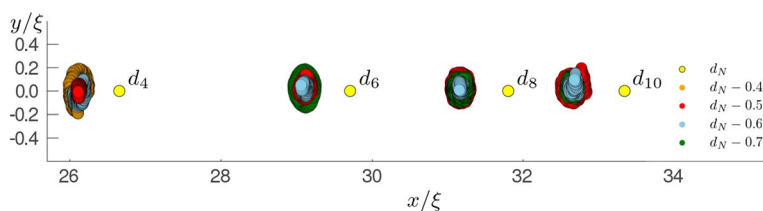
Fig. 7 Trajectories from GPE simulations of perturbed necklace states. Only the trajectories of the first vortex in each state are shown. d_4, d_6, d_8 and d_{10} mark the positions of the PVM stationary necklace state. To the left of each PVM stationary state marker are the trajectories of the first vortex in each state for different perturbed initial conditions (Color figure online)

stationary position is three perturbed GPE trajectories. The trajectories that had their initial positions perturbed from the PVM stationary position by -0.4 and -0.6 are shown in orange and sky-blue, respectively. These trajectories orbit a common center. The trajectory with initial position perturbed by -0.5 stays within a range of 0.1ξ from the duration of the simulation.

The GPE trajectories of the perturbed $N = 6$ necklace state are to the left of the d_6 yellow marker. The trajectory of the first vortex in the necklace perturbed inward by -0.6ξ from the PVM prediction is shown in sky-blue, and stays within a range of 0.1ξ over duration $t = 2000\xi/c$. Similarly, the perturbation of -0.6ξ from the PVM leads to a tight oscillation around the true stationary point for both the $N = 8$ and $N = 10$ necklace respectively. For necklace states with $N > 10$, the GPE trajectories become unstable on increasing shorter time scales.

References

1. H. Helmholtz, Lond. Edinb. Dubl. Philos. Mag. J. Sci. **33**(226), 485 (1867). https://doi.org/10.1080/14786446708639824
2. Gustav Robert Kirchhoff, *Vorlesungenüber Mathematische Physik: Mechanik*, vol. 1 (Teubner, Stuttgart, 1876)
3. E.A. Novikov, Zhurnal Eksperimental noi i Teoreticheskoi Fiziki **68**, 1868 (1975)
4. L. Onsager, Il Nuovo Cimento (1943–1954) **6**(2), 279 (1949). https://doi.org/10.1007/BF02780991
5. G. Gauthier, M.T. Reeves, X. Yu, A.S. Bradley, M.A. Baker, T.A. Bell, H. Rubinsztein-Dunlop, M.J. Davis, T.W. Neely, Science **364**(6447), 1264 (2019). https://doi.org/10.1126/science.aat5718
6. S.P. Johnstone, A.J. Groszek, P.T. Starkey, C.J. Billington, T.P. Simula, K. Helmerson, Science **364**(6447), 1267 (2019). https://doi.org/10.1126/science.aat5793
7. T.W. Neely, E.C. Samson, A.S. Bradley, M.J. Davis, B.P. Anderson, Phys. Rev. Lett. **104**(16), 160401 (2010). https://doi.org/10.1103/PhysRevLett.104.160401
8. K. Sasaki, N. Suzuki, H. Saito, Phys. Rev. Lett. **104**(15), 150404 (2010). https://doi.org/10.1103/PhysRevLett.104.150404
9. L.M. Pismen, *Vortices in Nonlinear Fields. From Liquid Crystals to Superfluids, from Non-Equilibrium Patterns to Cosmic Strings*, 1st edn. (Oxford University Press, New York, 1999)
10. A.S. Bradley, B.P. Anderson, Phys. Rev. X **2**(4), 041001 (2012). https://doi.org/10.1103/PhysRevX.2.041001
11. K. Henderson, C. Ryu, C. MacCormick, M.G. Boshier, New J. Phys. **11**(4), 043030 (2009). https://doi.org/10.1088/1367-2630/11/4/043030
12. G. Gauthier, I. Lenton, N.M. Parry, M. Baker, M.J. Davis, H. Rubinsztein-Dunlop, T.W. Neely, Optica **3**(10), 1136 (2016). https://doi.org/10.1364/OPTICA.3.001136

13. E.C. Samson, K.E. Wilson, Z.L. Newman, B.P. Anderson, Phys. Rev. A **93**(2), 023603 (2016). https://doi.org/10.1103/PhysRevA.93.023603

14. T. Aioi, T. Kadokura, T. Kishimoto, H. Saito, Phys. Rev. X **1**, 021003 (2011). https://doi.org/10.1103/PhysRevX.1.021003

15. M.T. Reeves, T.P. Billam, B.P. Anderson, A.S. Bradley, Phys. Rev. A **89**(5), 053631 (2014). https://doi.org/10.1103/PhysRevA.89.053631

16. T.P. Simula, M.J. Davis, K. Helmerson, Phys. Rev. Lett. **113**(16), 165302 (2014). https://doi.org/10.1103/PhysRevLett.113.165302

17. X. Yu, T.P. Billam, J. Nian, M.T. Reeves, A.S. Bradley, Phys. Rev. A **94**(2), 023602 (2016). https://doi.org/10.1103/PhysRevA.94.023602

18. X. Yu, A.S. Bradley, Phys. Rev. Lett. **119**(18), 185301 (2017). https://doi.org/10.1103/PhysRevLett.119.185301

19. M.M. Cawte, X. Yu, B.P. Anderson, A.S. Bradley, SciPost Phys. **6**(3), 032 (2019). https://doi.org/10.21468/SciPostPhys.6.3.032

20. A. Groszek, M. Davis, T. Simula, SciPost Phys. **8**(3), 039 (2020). https://doi.org/10.21468/SciPostPhys.8.3.039

21. M.T. Reeves, T.P. Billam, B.P. Anderson, A.S. Bradley, Phys. Rev. Lett. **110**(10), 104501 (2013). https://doi.org/10.1103/PhysRevLett.110.104501

22. H. Aref, Fluid Dyn. Res. **39**(1–3), 5 (2007). https://doi.org/10.1016/j.fluiddyn.2006.04.004

23. T.J. Stieltjes, Acta Math. **6**, 321 (1885). https://doi.org/10.1007/BF02400421

24. H. Aref, J. Fluid Mech. **290**(1), 167 (1995). https://doi.org/10.1017/S002211209500245X

25. M. Adler, J. Moser, Commun. Math. Phys. **61**(1), 1 (1978). https://doi.org/10.1007/BF01609465

26. J. Kim, A. Fetter, Phys. Rev. A **70**(4), 043624 (2004). https://doi.org/10.1103/PhysRevA.70.043624

27. L. Kurakin, J. Math. Fluid Mech. **7**(3), S376 (2005). https://doi.org/10.1007/s00021-005-0166-6

28. J.B. Kadtke, L.J. Campbell, Phys. Rev. A **36**(9), 4360 (1987). https://doi.org/10.1103/PhysRevA.36.4360

29. T. Bartsch, A. Pistoia, SIAM J. Appl. Math. **75**(2), 726 (2015). https://doi.org/10.1137/140981253

30. T. Bartsch, Q. Dai, J. Differ. Equ. **260**(3), 2275 (2016). https://doi.org/10.1016/j.jde.2015.10.002

31. C. Kuhl, J. Math. Anal. Appl. **433**(2), 1531 (2016). https://doi.org/10.1016/j.jmaa.2015.08.055

32. R. Navarro, R. Carretero-González, P.J. Torres, P.G. Kevrekidis, D.J. Frantzeskakis, M.W. Ray, E. Altuntaş, D.S. Hall, Phys. Rev. Lett. **110**(22), 225301 (2013). https://doi.org/10.1103/PhysRevLett.110.225301

33. L. Crasovan, G. Molina-Terriza, J. Torres, L. Torner, V. Perez-Garcia, D. Mihalache, Phys. Rev. E **66**(3), 036612 (2002). https://doi.org/10.1103/PhysRevE.66.036612

34. L. Crasovan, V. Vekslerchik, V. Perez-Garcia, J. Torres, D. Mihalache, L. Torner, Phys. Rev. A **68**(6), 063609 (2003). https://doi.org/10.1103/PhysRevA.68.063609

35. S. Middelkamp, P.J. Torres, P.G. Kevrekidis, D.J. Frantzeskakis, R. Carretero-González, P. Schmelcher, D.V. Freilich, D.S. Hall, Phys. Rev. A **84**(1), 011605 (2011). https://doi.org/10.1103/PhysRevA.84.011605

36. M. Mottonen, S. Virtanen, T. Isoshima, M. Salomaa, Phys. Rev. A **71**(3), 033626 (2005). https://doi.org/10.1103/PhysRevA.71.033626

37. S. Middelkamp, P.G. Kevrekidis, D.J. Frantzeskakis, R. Carretero-González, P. Schmelcher, Phys. Rev. A **82**(1), 013646 (2010). https://doi.org/10.1103/PhysRevA.82.013646

38. G. Theocharis, D.J. Frantzeskakis, P.G. Kevrekidis, B.A. Malomed, Y.S. Kivshar, Phys. Rev. Lett. **90**(12), 120403 (2003). https://doi.org/10.1103/PhysRevLett.90.120403

39. A.M. Barry, F. Hajir, P.G. Kevrekidis, J. Phys. A Math. Theor. **48**(15), 155205 (2015). https://doi.org/10.1088/1751-8113/48/15/155205

40. C.C. Lin, Proc. Nat. Acad. Sci. U.S.A. **27**(12), 570 (1941). https://doi.org/10.1073/pnas.27.12.570

41. C.C. Lin, Proc. Nat. Acad. Sci. **27**(12), 575 (1941). https://doi.org/10.1073/pnas.27.12.575

42. V.W. de Spinadel, Nonlinear Anal. Theory Methods Appl. **36**(6), 721 (1999). https://doi.org/10.1016/S0362-546X(98)00123-0

43. L.P. Pitaevskii, S. Stringari, *Bose–Einstein Condensation* (Clarendon Press, Oxford, 2003)

44. M. Reeves, Quantum Analogues of Two-Dimensional Classical Turbulence. Thesis, University of Otago (2017)

45. J. Bezanson, A. Edelman, S. Karpinski, V.B. Shah, SIAM Rev. **59**(1), 65 (2017). https://doi.org/10.1137/141000671

46. C. Tsitouras, Comput. Math. Appl. **62**(2), 770 (2011). https://doi.org/10.1016/j.camwa.2011.06.002

47. C. Rackauckas, Q. Nie, J. Open Res. Softw. **5**(1), 15 (2017). https://doi.org/10.5334/jors.151

48. A.S. Bradley, VortexDistributions.jl. (2019). https://github.com/AshtonSBradley/VortexDistribut ions.jl
49. A. Richaud, V. Penna, R. Mayol, M. Guilleumas, Phys. Rev. A **101**(1), 013630 (2020). https://doi.org/10.1103/PhysRevA.101.013630
50. P.K. Newton, *The N-Vortex Problem Applied Mathematical Sciences*, vol. 145 (Springer, New York, 2001). https://doi.org/10.1007/978-1-4684-9290-3

Publisher's Note Springer Nature remains neutral with regard to jurisdictional claims in published maps and institutional affiliations.